Hindawi
International Journal of Energy Research
Volume 2024, Article ID 8812313, 14 pages
https://doi.org/10.1155/2024/8812313

Research Article

Simulation of Radiation Damage and He Accumulation Induced by $^{10}B(n, \alpha)^{7}Li$ Reactions in Al-B_4C Neutron Absorbers Used in Spent Fuel Pools

Geon Kim,[1,2] **Myeongkyu Lee**,[1,3] **Yunsong Jung**,[1,4] **Eisung Yoon**,[1] **and Sangjoon Ahn**[1]

[1]*Department of Nuclear Engineering, Ulsan National Institute of Science and Technology, Ulju, Ulsan 44919, Republic of Korea*
[2]*KEPCO Nuclear Fuel, Daedeok-daero 989-242, Yuseong-gu, Daejeon 34057, Republic of Korea*
[3]*CCFE, Culham Science Centre, UKAEA (United Kingdom Atomic Energy Authority), Abingdon, Oxfordshire OX14 3DB, UK*
[4]*Korea Institute of Fusion Energy, Daejeon 34133, Republic of Korea*

Correspondence should be addressed to Eisung Yoon; esyoon@unist.ac.kr and Sangjoon Ahn; sjahn99@unist.ac.kr

Received 10 April 2023; Revised 3 December 2023; Accepted 6 December 2023; Published 6 January 2024

Academic Editor: Fatemeh Boshagh

Faster than expected surface corrosion and a considerable decrease in the ^{10}B areal density of a non-clad Al-B_4C neutron absorber were recently reported from surveillance coupons used in a spent fuel pool for about 8 years, which is only approximately one-fifth of the guaranteed service life of the absorber. Such premature degradation was largely attributed to irradiation-assisted corrosion since numerous gas bubbles filled with He and H were discovered in the Al alloy matrix near B_4C particles, and naturally $^{10}B(n, \alpha)^{7}Li$ reactions were designated as the underlying mechanism for the porosification that may have expedited the absorber corrosion. In this study, the levels of radiation damage and He concentration in the micrographs published in recent experimental studies were estimated to design ion beam irradiation experiments having appropriate parameters to emulate the status of neutron-irradiated non-clad Al-B_4C absorbers. TRITON, CSAS6, and SDTrimSP were coupled with modifications for the calculation of dpa and He concentration in irradiated neutron absorbers. The simulations yielded 3.74–6.71 dpa and 0.71–1.64 at% of He after 99 months of use and 3.82–8.39 dpa and 0.73–2.08 at% of He after 40 years of use. The simulations also demonstrated that the radiation damage and He concentration have a weak correlation with the particle diameter. In terms of radiation damage, these results are in good agreement with the reported experimental data, indicating that they can be referred to in the experimental design. The calculated He concentrations, however, may warrant modification to include leakage of implanted He atoms through irradiation-induced microcracks in the B_4C particles. Because of the high diffusivity of He, full leakage of He from B_4C particles to their boundaries with the Al alloy matrix was assumed for further estimations, which revealed that He concentration could be significantly elevated in the Al matrix near B_4C particles.

1. Introduction

High-density racks with neutron absorbers have been installed in spent fuel pools (SFPs) to maximize their packing density by allowing a reduced pitch between spent nuclear fuel (SNF) assemblies while maintaining criticality safety margins. Al-B_4C metal matrix composites (MMCs) are widely adopted as neutron absorber materials owing to the notably high thermal and epithermal neutron absorption cross section of ^{10}B [1–3]. In SFPs, the major sources of degradation of neutron absorbers have been considered to be exposure to the aqueous environment and gamma-ray radiation, as well as lesser levels of fast neutron irradiation. Thus, the service life of Al-B_4C MMC neutron absorbers has been generally guaranteed based on separate accelerated corrosion experiments and gamma-ray irradiation tests [4–7].

The integrity of the neutron absorbers has to be investigated throughout their service life to ensure their absorption

capability and the resulting safety margin of SFPs. However, once the neutron absorbers are installed in high-density racks during the fabrication process, the absorbers are sealed within the rack sheath and cannot be directly inspected throughout their service life [7, 8]. Instead, surveillance programs using coupons of the neutron absorbers have been commonly conducted to indicate the status of the neutron absorbers. In these programs, a series of surveillance coupons of neutron absorbers are placed in a storage cell surrounded by recently discharged SNF assemblies and periodically monitored for in-service investigation of the neutron absorber performance [9–11].

Recent studies [12, 13] observed significant surface corrosion of the surveillance coupons of a non-clad Al-B_4C MMC neutron absorber used for less than 9 years in an SFP, which was wholly inconsistent with the guaranteed 40 years of service life. Microstructure characterization of the surveillance coupons using transmission electron microscopy (TEM) and electron energy loss spectroscopy (EELS) revealed a porous microstructure with numerous locally formed voids and bubbles filled with He and H near B_4C particles [12]. This type of microstructure clearly exceeded the degree of degradation expected solely due to gamma-ray and fast neutron irradiation, considering their low fluence in SFPs [14–17].

A ^{10}B areal decrease (9.7% decrease over 99 months) and thickness reduction (3.7% decrease over 99 months) of the irradiated surveillance coupons also reported in the same studies revealed significant ^{10}B depletion as well as potential loss of B_4C particles in the surveillance coupons [12, 18]. Based on the observations, one of the previous studies [12] suggested that the premature degradation could be mainly attributed to a porosification of the Al matrix due to radiation damage and gas atom accumulation, which are induced by energetic He and Li ions from $^{10}B(n, \alpha)^7Li$ reactions given as

$$\begin{aligned} {}^{10}_{5}\mathrm{B} + {}^{1}_{0}n &\longrightarrow (94\%)\,{}^{7}_{3}\mathrm{Li}^{3+}(0.840\,\mathrm{MeV}) + {}^{4}_{2}\mathrm{He}^{2+}(1.470\,\mathrm{MeV}) \\ &+ \gamma(0.48\,\mathrm{MeV}) \longrightarrow (6\%)\,{}^{7}_{3}\mathrm{Li}^{3+}(1.015\,\mathrm{MeV}) \\ &+ {}^{4}_{2}\mathrm{He}^{2+}(1.777\,\mathrm{MeV}). \end{aligned} \tag{1}$$

While several studies on radiation shielding materials have been carried out [19–23], these investigations were not dedicated to the evaluation of the radiation damage induced by secondary energetic ions. Therefore, follow-up accelerated corrosion experiments on B_4C neutron absorbers need to be conducted to investigate and address the discrepancies between the current qualification test results and the new observations. These studies may perform charged-particle irradiation experiments in an accelerated manner, the design of which requires computational tools for the estimation of the accumulated radiation damage and He concentration in the neutron absorbers. A few experiments using charged-particle irradiation facilities have already been conducted on Al-B_4C MMC neutron absorbers to investigate their performance, but these studies employed empirically determined heavy ion doses [24–26]. Thus, computational estimation of the radiation damage and He atom accumulation by the newly considered MeV-level charged particles from $^{10}B(n, \alpha)^7Li$ reactions is required in order to more fully understand the degradation mechanism and certify the service life of neutron absorbers.

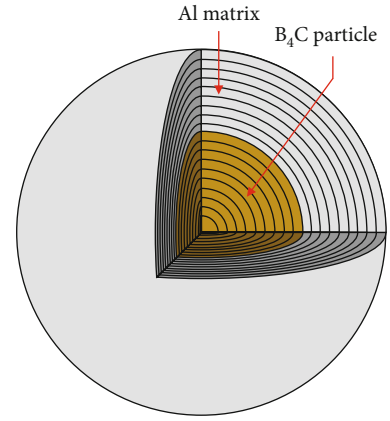

Figure 1: Example of the concentric shell configuration of a B_4C particle and Al matrix for simulation. The yellow central region and surrounding grey region represent the B_4C particle mesh and aluminum alloy mesh, respectively.

To reach the equivalent radiation damage and He concentration that were observed in the micrographs published in the recent experimental study [12], the same type of Al-B_4C surveillance coupon as used in previous experimental studies was simulated in this work with the objective to support future experimental emulations using ion beam accelerators. To investigate the B_4C particle size-dependent radiation damage and He concentration profiles near the particles, 10, 15, and 20 μm diameter, B_4C particles were assumed to be contained in the surveillance coupons. Additionally, several different coupon thickness reduction assumptions were considered, as a reduced thickness can result in a considerable change in the cumulative $^{10}B(n, \alpha)^7Li$ reactions in coupon peripheries. The simulations were conducted by SANTA [27], a dedicated code for the evaluation of radiation damage and ion distribution in Al-B_4C MMCs, which was developed by coupling several existing codes, Transport Rigor Implemented with Time-dependent Operation for Neutronic depletion (TRITON), Criticality Safety Analysis Sequence with KENO-VI (CSAS6), and Static and Dynamic Trim for Sequential and Parallel computer (SDTrimSP) [28, 29], with proper modifications to reflect the ion emission and geometric characteristics of B_4C particles.

2. Methods

2.1. $^{10}B(n, \alpha)^7Li$ Reaction Distribution. The Monte Carlo simulation codes based on binary collision approximation are generally utilized to evaluate the radiation damage and ion concentration resulting from interaction between incident energetic ions and materials. In such codes, the implanted ion position and displacements produced by the energetic ions are stochastically calculated based on the

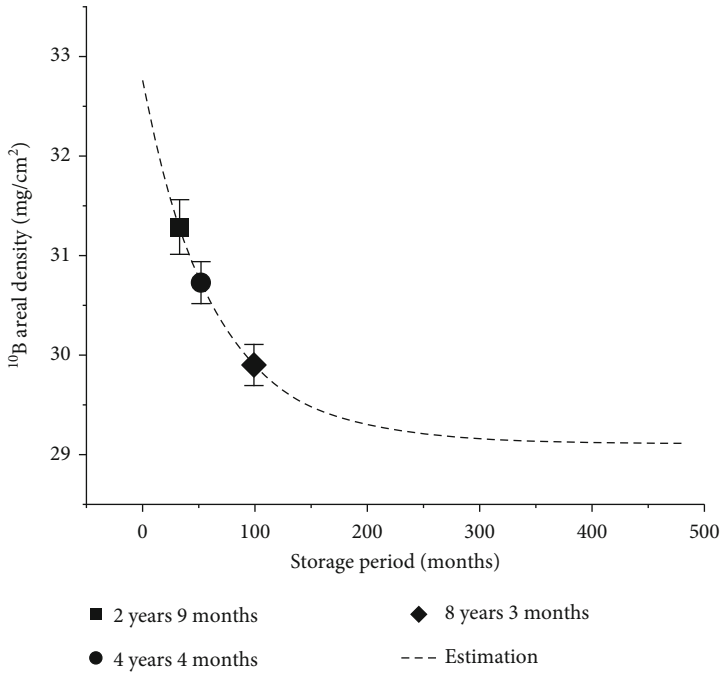

Figure 2: Estimation of ^{10}B areal density based on experimental data of a non-clad Al-B_4C MMC [18].

nature of the Monte Carlo method [29, 30]. Therefore, the number of Li and He ions produced from $^{10}B(n, \alpha)^7Li$ reactions within a B_4C particle should be provided beforehand.

The cumulative $^{10}B(n, \alpha)^7Li$ reactions in a single B_4C particle in a neutron absorber can be calculated on the basis of ^{10}B density change as below:

$$N_{(n,\alpha)} = \Delta n_{10_B} \times \frac{V_{\text{absorber}}}{N_{B_4C}}, \tag{2}$$

where $N_{(n,\alpha)}$ is the number of $^{10}B(n, \alpha)^7Li$ reactions per B_4C particle during neutron irradiation, Δn_{10_B} is the change in ^{10}B number density of the absorber, V_{absorber} is the volume of the absorber, and N_{B_4C} is the number of B_4C particles in the absorber. The change in the ^{10}B number density of an absorber, Δn_{10_B}, is given as

$$\Delta n_{10_B} = \frac{\Delta \rho_{A,10_B} \times N_A}{t \times M_{10_B}}, \tag{3}$$

where $\Delta \rho_{A,10_B}$ is the change in the areal density of ^{10}B in the neutron absorber, t is the thickness of the neutron absorber, N_A is Avogadro's number, and M_{10_B} is the molecular weight of ^{10}B.

The ^{10}B density, however, does not evenly decrease throughout the whole absorber since the $^{10}B(n, \alpha)^7Li$ reaction rate exponentially decreases along the absorber depth due to neutron attenuation. Thus, the neutron flux distribution within a surveillance coupon is calculated in advance using CSAS6, a Monte Carlo transport code in the SCALE code system, to reflect this distribution. In CSAS6 simulation, a surveillance coupon of the neutron absorber is divided into equal-volume cells in a structured grid along the depth direction. CSAS6 simulation requires the isotope concentration of the SNF assemblies, as surveillance coupons are generally surrounded by recently discharged SNF assemblies to expedite the degradation of the coupons [7, 8]. For this, the isotope concentration is provided at certain time instants using TRITON, a multipurpose code for transport and depletion.

Subsequently, the spatial distribution of the $^{10}B(n, \alpha)^7Li$ reaction rate and corresponding weighting factor for the reaction distribution of the cells are evaluated as below:

$$R^i = \sum_{g=1}^{N_{\text{group}}} \phi(g)^i \times \sum(g)^i_{(n,\alpha)}, \tag{4}$$

$$W^i = \frac{R^i}{\sum_{j=1}^{N_{\text{cell}}} R^j}, \tag{5}$$

where R^i is the $^{10}B(n, \alpha)^7Li$ reaction rate of coupon cell i, W^i is the weighting factor of coupon cell i, $\phi(g)^i$ is the neutron flux in coupon cell i for neutron energy group g, $\sum(g)^i_{(n,\alpha)}$ is the macroscopic cross section for $^{10}B(n, \alpha)^7Li$ reactions in coupon cell i for neutron energy group g, N_{group} is the number of neutron energy groups, and N_{cell} is the number of cells in the surveillance coupon. Therefore, the cumulative $^{10}B(n, \alpha)^7Li$ reactions $N^i_{(n,\alpha)}$ in a single B_4C particle in coupon cell i is given as

$$N^i_{(n,\alpha)} = W^i \times \Delta n_{10_B} \times \frac{V^i_{\text{cell}}}{N^i_{B_4C}}, \tag{6}$$

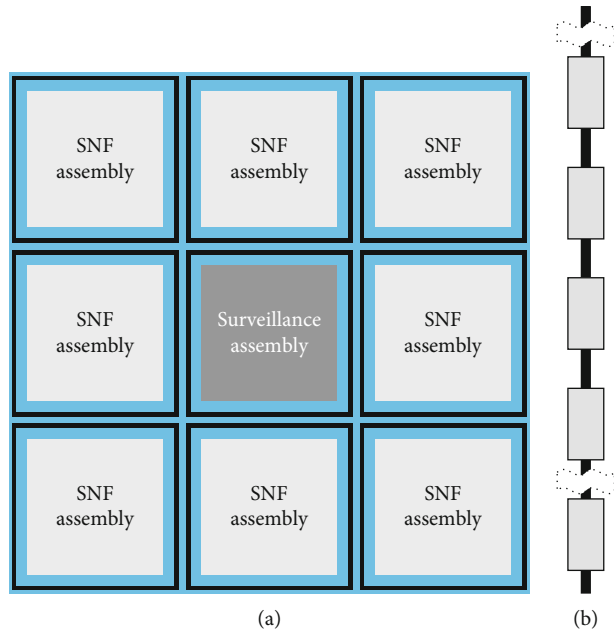

Figure 3: Schematic example of (a) a high-density rack configuration containing a surveillance assembly and (b) a surveillance assembly. To expedite the degradation of surveillance coupons, the surveillance assembly is generally surrounded by recently discharged SNF assemblies.

Table 1: Dimensions of the simulated surveillance coupons and SFP.

Parameter	Value
Assembly pitch (cm)	23.29
Rack height (cm)	453.39
Rack thickness (cm)	0.19
Surveillance coupon width (mm)	100 [12]
Surveillance coupon thickness (mm)	27 [12]
Surveillance coupon height (mm)	200 [12]
Absorber boron weight percent (wt%)	32.24 [12]
B_4C particle average size (μm)	5–9 [6]

where W^{i} is the weighting factor of coupon cell i, V^{i}_{cell} is the volume of coupon cell i, and $N^{i}_{B_4C}$ is the number of B_4C particles contained in coupon cell i. The weighting factor continuously varies throughout the absorber service life due to ^{10}B depletion in the absorber surface region. To reflect this variation, the Monte Carlo simulation for updating the weighting factor is repeated at every time instant. Then, Eq. (6) can be rewritten as below:

$$N^{i}_{(n,\alpha)} = \sum_{k=1}^{N_{step}} \Delta n^{k}_{10_B} \times W^{i,k} \times \frac{V^{i}_{cell}}{N^{i}_{B_4C}}, \quad (7)$$

where $\Delta n^{k}_{10_B}$ is the ^{10}B density change during time step k, $W^{i,k}$ is the weighting factor of coupon cell i at time step k, and N_{step} is the number of time steps.

The neutron-induced ^{10}B areal density decrease and the corresponding cumulative $^{10}B(n, \alpha)^{7}Li$ reactions in the coupon could be reduced by a decrease in coupon thickness, which is attributed to corrosion assisted by porous microstructures that are induced by irradiation. In this case, detachment of B_4C particles from the absorber surface due to severe corrosion largely contributes to the reduction of the ^{10}B areal density of the coupon. Accordingly, Eq. (7) should be updated as below:

$$N^{i}_{(n,\alpha)} = \sum_{k=1}^{N_{step}} \Delta n^{k}_{10_B} \times W^{i,k} \times V^{i,k}_{cell} \times \frac{F^{i,k}_{neutron}}{N^{i,k}_{B_4C}}, \quad (8)$$

where $V^{i,k}_{cell}$ is the volume of coupon cell i at time step k, $F^{i,k}_{neutron}$ is the fraction of neutron-induced ^{10}B areal density decrease for coupon cell i at time step k, and $N^{i,k}_{B_4C}$ is the number of B_4C particles contained in coupon cell i at time step k.

2.2. Ion Implantation and Vacancy Production. B_4C particles contained in B_4C-Al MMCs have sphere-like geometry with faceted surfaces. However, for simplifying the problem, the shape of the B_4C particles is assumed here to be a perfect sphere. Then, a B_4C particle and surrounding Al matrix are divided into several concentric shells, as shown in Figure 1. Also, the angular dependency of neutron flux within the B_4C particle is ignored since the mean particle size (5–9 μm) [6] is over 20-fold smaller than the mean free path of a thermal neutron in a B_4C particle (~120 μm). By exploiting the above two assumptions, the calculation of radiation damage and He accumulation simplifies to a problem with spherical symmetry.

The spatial distributions of radiation damage and He concentration are calculated with the given number of

Table 2: Chemical composition of a non-clad Al-B_4C MMC [6].

Element	Composition (wt%)
6061 Al powder	
Mg	0.080–1.20
Si	0.40–0.80
Cu	0.15–0.40
Fe	0.15 (max.)
Zn	0.25 (max.)
Ti	0.15 (max.)
Ni	50 ppm (max.)
Co	10 ppm (max.)
Mn	10 ppm (max.)
Cr	10 ppm (max.)
Al	Bal.
ASTM C750 Type 1 B_4C powder	
Total B	76.50 (min.)
Total B+C	98.0
^{10}B	19.90 ± 0.3 at%
HNO_3 sol. B	0.59 (max.)
H_2O sol. B	0.29 (max.)
Si	0.50 (max.)
Fe	0.50 (max.)
Ca	0.30 (max.)
F	25 ppm (max.)
Cl	57 ppm (max.)

emitted ions in aB_4C particle using SDTrimSP, which can simulate the interaction between incident energetic charged particles and lattice atoms [29]. SDTrimSP was provided from the Max-Planck-Institut für Plasmaphysik in Germany. The original version of SDTrimSP, however, was designed for a one-dimensional Cartesian coordinate system. In the code, all layers are treated as infinite planes, and hence, it can only support parallel incident ions [31–33]. Therefore, we modified SDTrimSP to consider the simultaneous emission of energetic ions from the entire bulk of B_4C particles and a spherical geometry.

As the first step, a spherical coordinate system is applied to deal with the curved surface of a B_4C particle. In the modified SDTrimSP, the position of ions and produced vacancies are automatically converted from Cartesian coordinates to spherical coordinates; the positions of ions and all displacement data are stored and processed in radial coordinates under the spherical symmetry assumption. Second, multipoint ion irradiation is included to reflect simultaneously emitted ions over the entire region of the B_4C particle. The modified SDTrimSP sets the start positions of the trajectories of the He and Li ions to the midpoint of the B_4C particle shells (see Figure 1), and it selects the starting point shell based on the $^{10}B(n, \alpha)^7Li$ reaction distribution within the B_4C particle.

The number of displacements and implanted ions in the concentric shells of the B_4C particles and Al matrix can then be properly calculated with the above modifications. The effective number of generated displacements is evaluated using the Norgett-Robinson-Torrens model [34]. The displacement energies of B, C, and Al are, respectively, set to 46, 69, and 25 eV, following the recommendation of Konobeyev et al. and ASTM E521 [35, 36] for direct comparison with experimental studies utilizing the code. The total number of produced displacements is converted into dpa units by dividing them by the number of lattice atoms (B, C, and Al) in each shell. Therefore, the dpa value largely depends on the atomic fraction of the lattice atoms and likely increases with ion implantation.

Charged heavy particles (He and Li ions) produced in the central region of B_4C particles are mostly stopped within the particle due to their short ranges in the B_4C medium (1–4 μm). As a result, radiation damage and He atoms can concentrate in the intraparticle region and possibly form a porous structure. In this region, gas atom accumulation could increase the range of heavy ions by decreasing the macroscopic stopping power of the material, which could expand the radiation-damaged Al areas over the course of potentially extended service times. Hence, the neutron flux distribution in the intraparticle region has to be appropriately evaluated beforehand. The result of a one-group neutron diffusion equation for a nonmultiplying system indicated negligible neutron attenuation along the particle radius because of the extremely small B_4C particle sizes. A simple Monte Carlo simulation reaffirmed this minor attenuation even for a particle of 40 μm radius, which is over 8 times larger than the mean size of the particles in a non-clad Al-B_4C MMC. Therefore, the $^{10}B(n, \alpha)^7Li$ reactions are assumed to take place uniformly over the B_4C particle bulk.

The rigorous dynamic mode of SDTrimSP that continuously updates the atomic fraction of the layers is activated to reflect the aforementioned ion range extension due to porosification [29]. Based on the positions of the implanted ions (He and Li) and consequently displaced lattice atoms, SDTrimSP reevaluates the atomic fractions at every time step. The number density of He atoms in the materials is referred from the measured He number density in a 5 nm bubble in Al matrix using EELS [37]: the number density of He atoms is 4.2×10^{28} m^3 at 300 K with a compressibility factor of 2.2 (pressure is estimated as approximately 400 MPa).

3. Results and Discussion

3.1. Cumulative $^{10}B(n, \alpha)^7Li$ Reactions per B_4C Particle. The ^{10}B areal density decrease of the coupons through their operation was acquired by referring to the dataset from the previous study by Jung et al. [12, 18]. Figure 2 shows the estimation of ^{10}B areal density reduction along irradiation time based on experimental measurements. The previous studies fitted the data by an exponential function with an R-squared value of 0.9999 and estimated a ^{10}B depletion of 11.6% over the 40-year service life. The fitted ^{10}B depletion with irradiation time was given as

$$\rho_A^{10_B}(t) = y_0 + A \bullet e^{-(t-t_0)/B_1} + A \bullet e^{-(t-t_0)/B_2}, \quad (9)$$

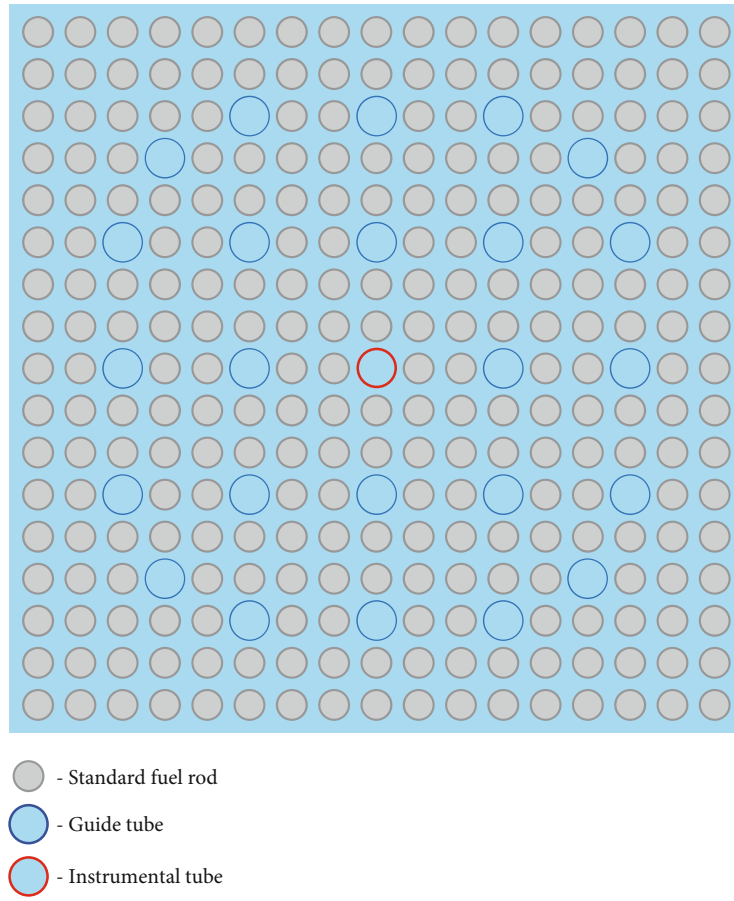

Figure 4: Schematic illustration of the 17 × 17 lattice geometry of the EC45 assembly [38, 39]. The assembly comprises 264 standard fuel rods and 25 guide/instrumental tubes.

where $\rho_A^{^{10}B}(t)$ is the ^{10}B areal density (mg/cm^2) with irradiation time t (month), y_0 is 29.1265, A is 1.08029, t_0 is 33, B_1 is 57.8511, and B_2 is 70.7069 [12, 18].

The CSAS6 code simulated the surveillance coupons located in the center of one storage cell surrounded by recently discharged SNF assemblies, as shown in Figure 3(a). In the simulation, 8 surveillance coupons of a non-clad neutron absorber were axially bundled into a surveillance assembly, an example of which is shown in Figure 3(b), to account for the axial neutron flux distribution induced by the boundary effect and the axial burnup profile of the SNF. The dimensions of the simulated surveillance coupon and the SFP are specified in Table 1. The chemical compositions of high-purity Al 6061 alloy and nuclear-grade boron carbide powder (ASTM C750 Type 1), the materials composing the non-clad Al-B_4C MMC, are given in Table 2 [6].

The surveillance coupons were divided into 10 cells to reflect the neutron flux distribution along the depth direction. The Monte Carlo simulation of the SFP was conducted at time instants of 0, 100, 1000, 2000, 4000, 8000, and 12000 days to evaluate long-term neutron flux variation, and hence, the isotope composition in the assembly was also calculated at these time instants. In this study, the recently discharged assembly EC45 having a burnup of 52,584 MWD/MTU, the configuration of which is shown in Figure 4, was assumed to be charged in surrounding storage cells of the SFP, with a concentration of boric acid in the coolant of 2000 ppm. The design parameters of the assembly are summarized in Table 3 [38, 39].

Table 3: Design parameters of the EC45 assembly [38, 39].

Parameter	Value
Lattice geometry	17 × 17
Fuel rod pitch (cm)	1.26
Assembly pitch (cm)	21.504
Active fuel rod length (cm)	365.76
Fuel material type	UO_2
Fuel pellet density (%TD)	96.016
Fuel pellet diameter (cm)	0.8191
Enrichment (wt%)	4.4982
Clad material type	ZIRLO
Clad inner diameter (cm)	0.8356
Clad outer diameter (cm)	0.950

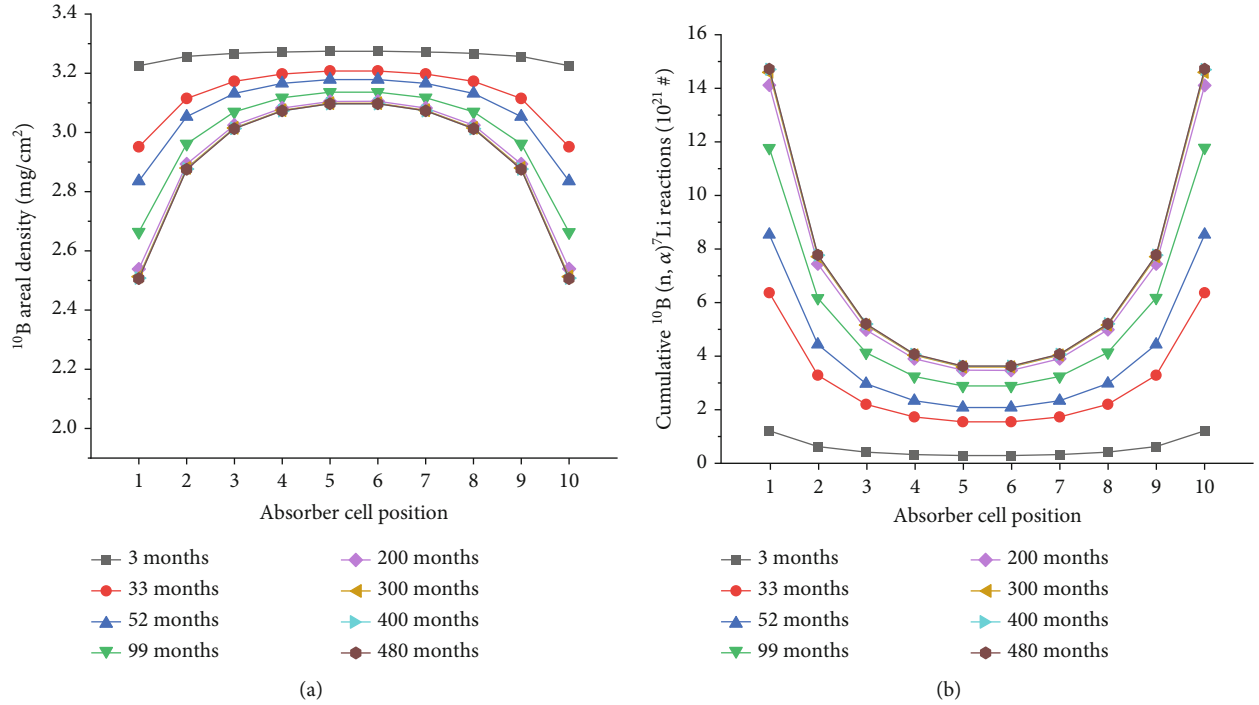

Figure 5: (a) ^{10}B areal density distribution along the neutron absorber depth for the no corrosion case and (b) corresponding cumulative ^{10}B(n, α)^{7}Li reactions of the coupon cells.

The axial positions of the degraded surveillance coupons were undefined in the previous study by Jung et al. [12]. However, considering the severe surface corrosion, the coupons were speculated in the present work to be located in the middle of the surveillance assembly, where they experience the highest neutron flux. The Monte Carlo simulation results indicated that the fifth surveillance coupon from the bottom, which is the nearest one to the center of the active fuel, was subjected to the most severe neutron radiation.

As corrosion-induced B_4C particle loss could largely contribute to the ^{10}B areal density reduction, 3 cases of corrosion were considered in the simulations: no corrosion over the whole service life, corrosion until the latest observation (99 months), and corrosion until near the end of the service life (400 months). In the simulations, the coupon thickness data reported in Jung et al. [12] was employed: 1.48% and 3.70% decrease after 52 months and 99 months of irradiation, respectively.

When the thickness reduction due to corrosion was neglected (no corrosion case), the simulation yielded a considerable ^{10}B number density decrease at the peripheries of the coupon, approximately 4 times greater than that at the center and 2 times greater than the average density decrease during the 40-year service life. Figure 5(a) shows the calculated ^{10}B number density distribution of the coupon cells stacked along the depth direction at several time instants. As shown in the figure, the ^{10}B areal densities of the outermost cells rapidly decreased with irradiation time. The corresponding cumulative ^{10}B(n, α)^{7}Li reactions of the coupon cells are displayed in Figure 5(b).

The simulation was subsequently conducted for the coupon with a thickness decrease of 3.70% after 99 months but was stopped from this point, the so-called "corrosion until 99 months" case. Based on the previous measurement, the thickness of the coupon was set to decrease from 0.27 cm to 0.26 cm over 99 months, as plotted with the red line in Figure 6. Figure 7(a) displays the ^{10}B areal density distribution within the coupon, showing that the ^{10}B areal densities of the cells at the peripheries largely decreased compared to the no corrosion case. However, as shown in Figure 7(b), the cumulative ^{10}B(n, α)^{7}Li reactions in those cells were in fact

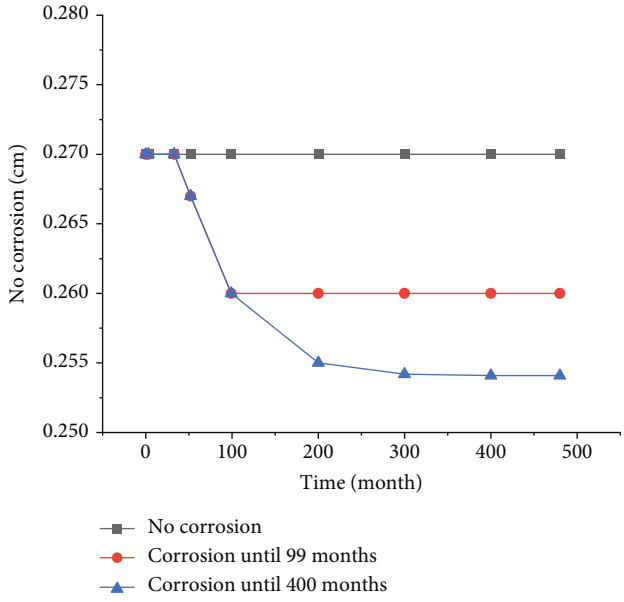

Figure 6: Coupon thickness with elapsed irradiation time in the simulations.

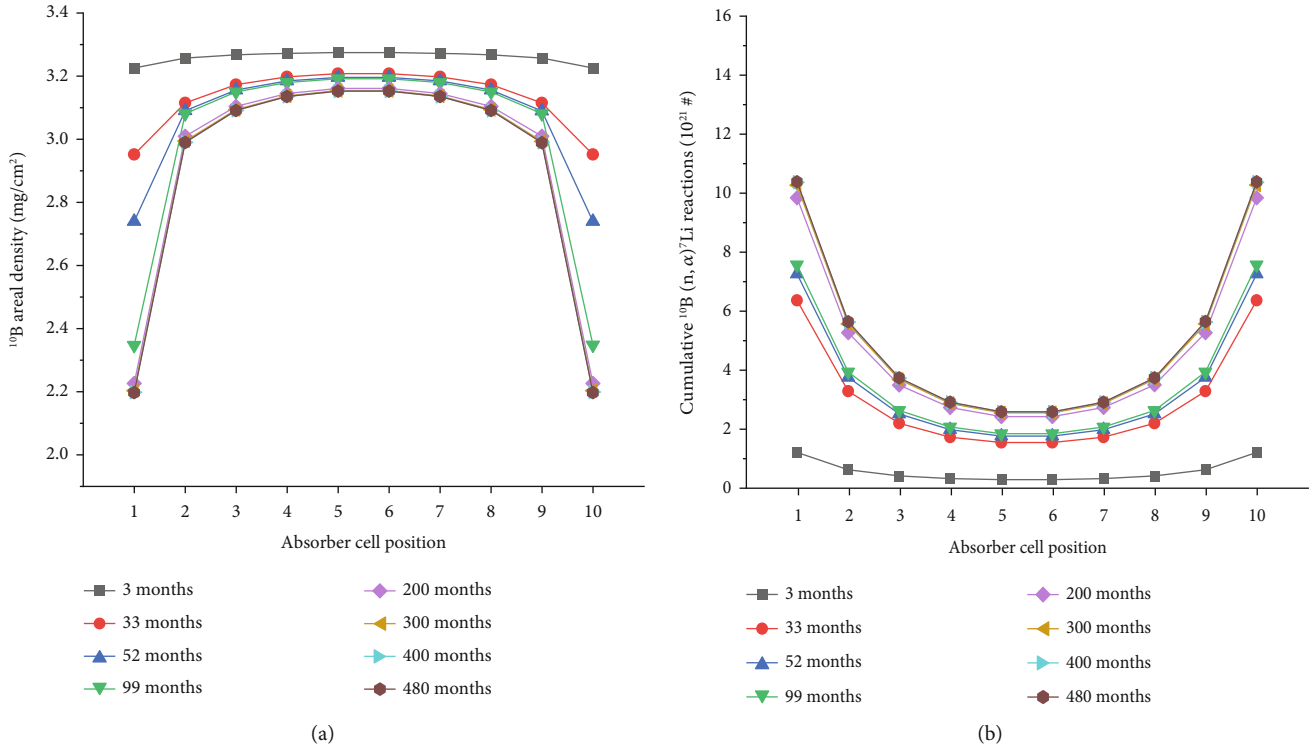

FIGURE 7: (a) ^{10}B areal density distribution along the neutron absorber depth for the corrosion until 99 months case and (b) corresponding cumulative ^{10}B(n, α)^{7}Li reactions of the coupon cells.

reduced since a considerable amount of the ^{10}B areal density reduction resulted from the loss of B_4C particles.

This tendency was further exacerbated in the "corrosion until 400 months" case. Here, the coupon thickness was assumed to decrease to 0.254 cm over the 400 months of operation time, as plotted with the blue line in Figure 6. The coupon thickness with operation time was determined based on the ^{10}B areal density reduction due to the ^{10}B(n, α)^{7}Li reactions; this neutron-induced ^{10}B areal density decrease during each time step was forced to follow the exponential decrease in the number of neutrons produced from the SNF assemblies with decay time. The ^{10}B areal densities of the coupon cells in this case are displayed in Figure 8(a) with irradiation time. In the outermost cells, the ^{10}B areal densities drastically decrease since a large number of B_4C particles were assumed to be swept away to the coolant from the coupon surface. However, as shown in Figure 8(b), for the same reason as in the former case, the cumulative ^{10}B(n, α)^{7}Li reactions in the outermost cells reduce to about half compared to those of the no corrosion case.

For the outermost cells, which need to be experimentally investigated as they have been subjected to severe corrosion, the cumulative ^{10}B(n, α)^{7}Li reactions per coupon cell after 40 years of irradiation were calculated to be 14.72×10^{21} for the no corrosion case, 10.39×10^{21} for the corrosion until 99 months case, and 8.07×10^{21} for the corrosion until 400 months case. After 99 months of irradiation, the cumulative ^{10}B(n, α)^{7}Li reactions per cell were estimated to be 1.18×10^{22} for the no corrosion case and 7.57×10^{21} for the corrosion until 99 months case, respectively.

The cumulative ^{10}B(n, α)^{7}Li reactions were divided by the number of contained B_4C particles in the cell to provide the number of emitted atoms for the calculation of radiation damage and He accumulation (see Eq. (8)). The absorber manufacturer informed the mean diameter of B_4C particles to be 5–9 μm [6]. However, various sizes of B_4C particles could be included in the neutron absorbers during fabrication; hence, simulations of radiation damage and He accumulation were conducted for 10, 15, and 20 μm diameter B_4C particles. Tables 4 and 5, respectively, show the number of ^{10}B(n, α)^{7}Li reactions per B_4C particle for 99 months and 40 years of operation. As shown in the tables, the cumulative ^{10}B(n, α)^{7}Li reactions per B_4C particle are proportional to the particle volume since the simulation neglected neutron attenuation along the radius direction.

3.2. Radiation Damage and He Concentration in Surveillance Coupons. Radiation damage and ion distribution were calculated for 10, 15, and 20 μm diameter particles having various numbers of B_4C particle shells and 50 surrounding Al shells (see Figure 1). The Al shells were set to have 0.2 μm intervals, and therefore, all emitted He and Li ions having short ranges in Al matrix (2–6 μm) are sufficiently confined in the Al matrix layers (10 μm) without transmission.

Figure 9 shows the radiation damage in dpa units and He atom concentration in at% units within the Al matrix beyond the particle-matrix interface for the 3 corrosion cases after 40-year irradiation time. The maximum radiation damage and He concentration were 3.82–8.39 dpa and 0.73–2.08 at%, respectively, depending on the corrosion

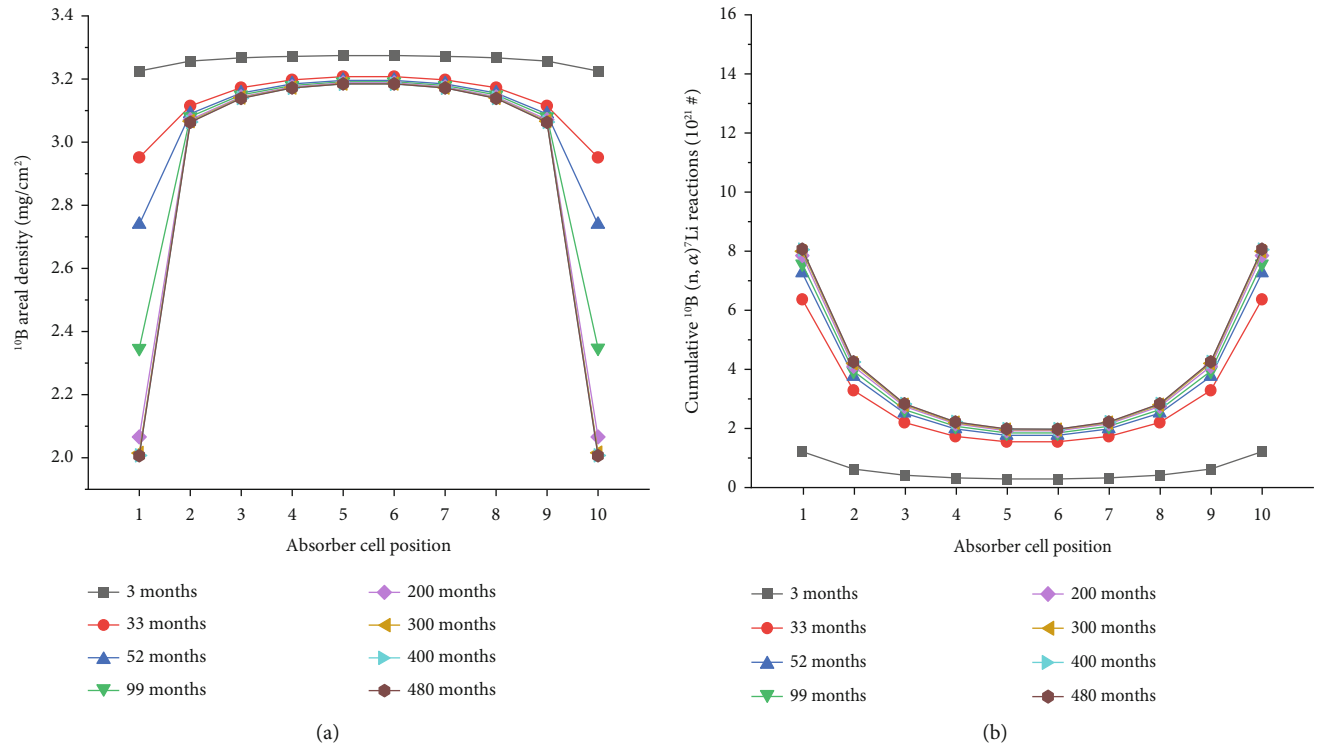

Figure 8: (a) ^{10}B areal density distribution along the neutron absorber depth for the corrosion until 400 months case and (b) corresponding cumulative ^{10}B(n, α)^{7}Li reactions of the coupon cells.

Table 4: Cumulative number of ^{10}B(n, α)^{7}Li reactions per B_4C particle over 40 years in the 3 considered cases.

Diameter	No corrosion	Corrosion until 99 months	Corrosion until 400 months
10 μm	2.73×10^{12}	2.06×10^{12}	1.54×10^{12}
15 μm	9.20×10^{12}	6.96×10^{12}	5.19×10^{12}
20 μm	2.18×10^{13}	1.65×10^{13}	1.23×10^{13}

Table 5: Number of cumulative ^{10}B(n, α)^{7}Li reactions per B_4C particle over 99 months in 2 considered cases.

Diameter	No corrosion	Corrosion until 99 months
10 μm	2.18×10^{12}	1.42×10^{12}
15 μm	7.36×10^{12}	4.81×10^{12}
20 μm	1.74×10^{13}	1.14×10^{13}

assumption and the diameter. The radiation damage and He atom concentration in the surveillance coupons irradiated for 99 months were calculated as 3.73–6.71 dpa and 0.71–1.64 at%, respectively, as shown in Figure 10. The radiation damage of the irradiated coupons for the 99 months case is well matched with former estimates (1–10 dpa) [18, 25] and therefore can provide a viable benchmark for the level of radiation damage that results in the morphology observed in the previous study [12]. Nonetheless, it is worthwhile to note that the He atom concentration could differ from the actual case due to thermal spike and ballistic collision, which enhance the high mobility of He atoms in the medium.

Both radiation damage and He atom concentration in the Al matrix rapidly decreased until a distance of about2.5 μm from the particle-matrix interface since the ranges of Li ions in Al are approximately 2.27 and 2.60 μm for energies of 0.84 and 1.015 MeV, respectively. The results then showed a slow decrease in radiation damage until a distance of about 5 μm from the interface since the ranges of He ions in Al are approximately 4.65 and 5.70 μm for energies of 1.47 and 1.777 MeV, respectively. Therefore, vacancies produced by Li ions are likely concentrated within roughly 2.5 μm from the interface. Implanted Li ions also contribute to the elevation in radiation damage near the interface by reducing the atomic fraction of the lattice Al atoms.

With an increase in diameter, both radiation damage and He atom concentration results slightly increased due to the increase in the cumulative ^{10}B(n, α)^{7}Li reactions per B_4C particle. However, because of the shallow penetration depth of heavy ions in the B_4C medium, the thickness of the B_4C particle region that can affect the Al matrix is restricted to a few μm from the interface, and hence, most of the emitted heavy ions are likely stopped within the B_4C. As displayed in Figures 9 and 10, the calculated maximum radiation damage near the 20 μm diameter B_4C particle is only about 25% higher than the result of the 10 μm diameter particle since more than 70% of the produced ions from the 20 μm diameter particle are retained in the B_4C particle region due to their short range in B_4C medium.

Considering the many irradiation-induced microcracks and the bubble-free microstructure of the B_4C particles found in the previous study [12], high-diffusivity He atoms

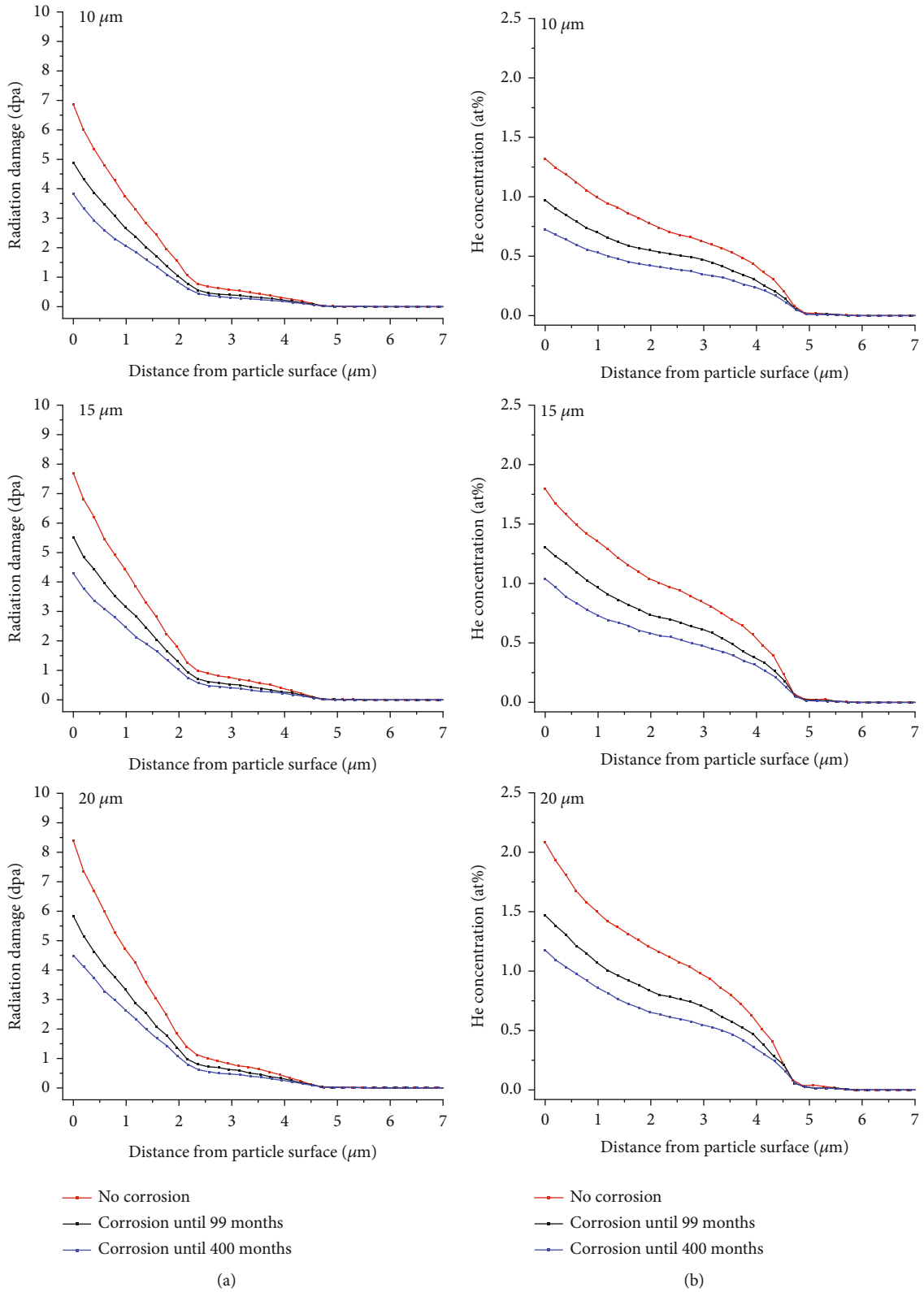

Figure 9: (a) Radiation damage and (b) He concentration in the Al matrix near B_4C particles with diameters of 10, 15, and 20 μm after 40 years.

in the B_4C region would likely leak out through the microcracks and be concentrated near the B_4C particle surface. Accordingly, in actual cases, local He concentration and porosity at the particle-matrix interface could be significantly higher than the simulation results: according to simple calculations, possibly more than 30 at% of He can be achieved near 20 μm diameter B_4C particles if all implanted He atoms leak to the adjacent Al matrix layer. This excessive

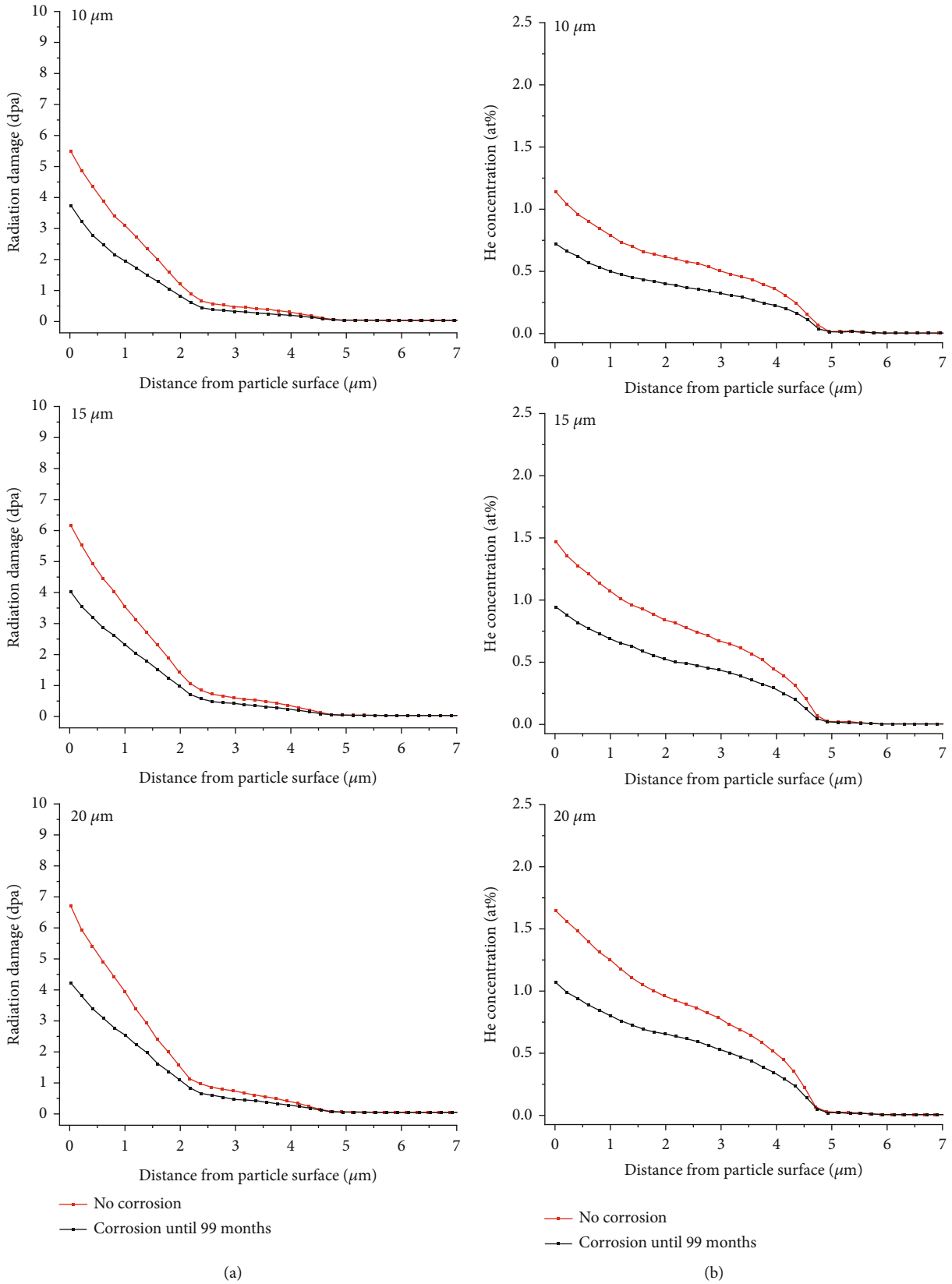

Figure 10: (a) Radiation damage and (b) He concentration in the Al matrix near B_4C particles with diameters of 10, 15, and 20 μm after 99 months.

He concentration can largely assist the irradiation-induced bubble formation and growth in conjunction with remnant H atoms [40–43] produced by severe surface corrosion. This porosification would likely propagate along the boundaries between B_4C particles and Al matrix, which could lead to the detachment of B_4C particles and thus the early depletion of ^{10}B and subsequent increase in the criticality of the pool.

4. Conclusion

The equivalent radiation damage and He concentration reached in the recently reported surveillance coupons of a non-clad Al-B_4C metal matrix composite neutron absorber used in a spent fuel pool were evaluated by coupling TRITON, CSAS6, and modified SDTrimSP codes to inform the design of ion beam irradiation experiments that emulate the irradiation-induced microstructures of the absorbers. The simulations yielded 3.74–6.71 dpa and 0.71–1.64 at% of He for 99 months of irradiation and 3.82–8.39 dpa and 0.73–2.08 at% of He for 40 years of irradiation as the maximum radiation damage and He concentration in the Al matrix near 10, 15, and 20 μm diameter B_4C particles.

More than 70% of the produced He ions emitted from the 20 μm diameter B_4C particles could not reach the Al matrix but rather were retained within the B_4C particle region due to the short ranges of He and Li ions in B_4C medium. Hence, the estimated radiation damage and He concentration within the Al matrix surrounding B_4C particles of different sizes showed very weak dependence on the particle size, even though the total number of cumulative $^{10}B(n, \alpha)^7Li$ reactions per B_4C particle was almost linearly proportional to the particle volume. However, due to the high diffusivity of He and numerous irradiation-induced microcracks in the B_4C particles, a significant portion of implanted He atoms could leak to the boundary between the particles and Al matrix, especially near large B_4C particles. The synergistic effects of locally concentrated He and H, the latter of which is generated from surface corrosion, can largely assist bubble formation and growth and consequently severe porosification [40–45]. Therefore, to experimentally emulate a neutron-irradiated Al-B_4C absorber, various levels of He implantation should be considered at the experimentalists' discretion, perhaps between the lower bound (ballistically escaped He) and the upper bound (all He produced for the B_4C particle under consideration) estimated from simulations.

The radiation damages calculated in this work were well matched with the experimental estimations that can be found in the literature, and thus, these values can be directly referred to in experimental designs for the emulation of irradiation-assisted corrosion of such type of neutron absorbers.

Data Availability

The simulation data used to support the findings of this study are included within the article.

Conflicts of Interest

The authors declare that they have no conflicts of interest.

Authors' Contributions

Geon Kim was responsible for the investigation, visualization, software, formal analysis, and data curation; wrote the original draft; and wrote, reviewed, and edited the manuscript. Myeongkyu Lee carried out the investigation, methodology, and validation. Yunsong Jung assisted in the investigation, methodology, and validation. Eisung Yoon was responsible for the software, resources, project administration, funding acquisition and wrote, reviewed, and edited the manuscript. Sangjoon Ahn assisted in the conceptualization, project administration, funding acquisition, and supervision and wrote, reviewed, and edited the manuscript.

Acknowledgments

The authors would like to thank A. Mutzke at Max-Planck-Institut für Plasmaphysik for providing the SDTrimSP code. This research was supported by a National Research Foundation of Korea (NRF) grant funded by the Korean government (Ministry of Science and ICT) (grant numbers RS-2022-00155991 and NRF-2019M2D2A1A01059543) and by the Nuclear Safety Research Program through the Korea Foundation Of Nuclear Safety (KoFONS) using financial resources granted by the Nuclear Safety and Security Commission (NSSC) of the Republic of Korea (grant number 2103084).

References

[1] H. Akkurt, A. Quigley, and M. Harris, "Update on accelerated corrosion tests for the evaluation of long-term performance of BORAL® in spent fuel pools," *Transactions of the American Nuclear Society*, vol. 117, pp. 319–322, 2022.

[2] A. Machiels and R. Lambert, *Handbook of Neutron Absorber Materials for Spent Nuclear Fuel Transportation and Storage Applications*, 2009.

[3] A. Machiels and R. Lambert, *Qualification Testing for Metal Matrix Neutron Absorber Materials for Wet & Dry Storage Applications*, Electric Power Research Institute, Palo Alto, CA, 2006.

[4] M. L. Eyre, D. Nagasawa, T. Yamazaki, and A. C. Herfurth, "5-year accelerated corrosion testing of MAXUS® for spent fuel pool and dry cask performance," in *Proceedings of the 19th International Symposium on the Packaging and Transportation of Radioactive Materials, PATRAM*, New Orleans, LA, USA, 2019.

[5] Electric Power Research Institute, *Qualification of METAMIC® for spent-fuel storage application*, EPRI, Palo Alto, CA, 2001, 1003137.

[6] Holtec International, *Use of Metamic® in fuel pool applications*, Marlton, NJ, USA, 2015, HI-2022871.

[7] Electric Power Research Institute, *Accelerated corrosion testing of BORAL®*, Palo Alto, CA, 20091018911.

[8] Electric Power Research Institute, *Strategy for managing the long term use of BORAL® in spent fuel storage pools*, Palo Alto, CA, 20121025204.

[9] Electric Power Research Institute, *Overview of BORAL® performance based upon surveillance coupon measurements*, Palo Alto, CA, 20101021052.

[10] Northeast Technology Corp, *Inspection and Testing of BORAL® and Fast Start Surveillance Coupons from the LaSalle County Units 1 & 2 Stations*, Kingston, NY, USA, 2009.

[11] United States Nuclear Regulatory Commission, *Material Qualification Report of MAXUS® for Spent Fuel Storage, ML15336A084*, Washington, DC, USA, 2015.

[12] Y. Jung, M. Lee, K. Kim, and S. Ahn, "10B (n, α) 7Li reaction-induced gas bubble formation in Al–B4C neutron absorber irradiated in spent nuclear fuel pool," *Journal of Nuclear Materials*, vol. 533, article 152077, 2020.

[13] K. Kim, S. Chung, and J. Hong, "Performance evaluation of METAMIC neutron absorber in spent fuel storage rack," *Nuclear Engineering and Technology*, vol. 50, no. 5, pp. 788–793, 2018.

[14] N. C. Tam and L. Lakosi, "Monitoring fast neutron flux inside spent reactor fuel by CR-39 detector," *Radiation Measurements*, vol. 34, no. 1-6, pp. 601–603, 2001.

[15] L. Lakosi and C. T. Nguyen, "Gamma and fast neutron radiation monitoring inside spent reactor fuel assemblies," *Nuclear Instruments and Methods in Physics Research Section A: Accelerators, Spectrometers, Detectors and Associated Equipment*, vol. 580, no. 1, pp. 788–791, 2007.

[16] International Atomic Energy Agency, *Storage of water reactor spent fuel in water pools*, vol. 218, 1982Vienna, Austria, 1982.

[17] International Atomic Energy Agency, *Understanding and managing ageing of material in spent fuel storage facilities*, vol. 443, 2006Vienna, Austria, 2006.

[18] Y. Jung, *10B(n, α)7Li Reaction Accelerated Degradation of Al-B4C Neutron Absorber Used in Spent Nuclear Fuel Pool, [Ph.D. thesis]*, Ulsan National Science and Technology, 2020, https://scholarworks.unist.ac.kr/handle/201301/53737.

[19] H. H. Hegazy, M. S. Al-Buriahi, F. Alresheedi, S. Alraddadi, H. Arslan, and H. Algarni, "The effects of TeO_2 on polarizability, optical transmission, and photon/neutron attenuation properties of boro-zinc-tellurite glasses," *Journal of Inorganic and Organometallic Polymers and Materials*, vol. 31, no. 6, pp. 2331–2338, 2021.

[20] H. H. Hegazy, M. S. Al-Buriahi, F. Alresheedi et al., "Nuclear shielding properties of B_2O_3–Bi_2O_3–SrO glasses modified with Nd_2O_3: theoretical and simulation studies," *Ceramics International*, vol. 47, no. 2, pp. 2772–2780, 2021.

[21] I. Boukhris, I. Kebaili, M. S. Al-Buriahi, A. Alalawi, A. S. Abouhaswa, and B. Tonguc, "Photon and electron attenuation parameters of phosphate and borate bioactive glasses by using Geant4 simulations," *Ceramics International*, vol. 46, no. 15, pp. 24435–24442, 2020.

[22] M. S. Al-Buriahi, V. P. Singh, H. Arslan, V. V. Awasarmol, and B. T. Tonguc, "Gamma-ray attenuation properties of some NLO materials: potential use in dosimetry," *Radiation and Environmental Biophysics*, vol. 59, no. 1, pp. 145–150, 2020.

[23] M. S. Al-Buriahi, C. Eke, S. Alomairy, C. Mutuwong, and N. Sfina, "Micro-hardness and gamma-ray attenuation properties of lead iron phosphate glasses," *Journal of Materials Science: Materials in Electronics*, vol. 32, no. 10, pp. 13906–13916, 2021.

[24] F. Zhang, J. B. Wierschke, X. Wang, and L. Wang, "Nanostructures formation in Al-B_4C neutron absorbing materials after accelerated irradiation and corrosion tests," *Microscopy and Microanalysis*, vol. 21, no. S3, pp. 1159-1160, 2015.

[25] F. Zhang, X. Wang, J. B. Wierschke, and L. Wang, "Helium bubble evolution in ion irradiated Al/B_4C metal metrix composite," *Scripta Materialia*, vol. 109, pp. 28–33, 2015.

[26] Y. Jung, Y. Lee, J. H. Kim, and S. Ahn, "Accelerated corrosion tests of Al-B_4C neutron absorber used in spent nuclear fuel pool," *Journal of Nuclear Materials*, vol. 552, article 153011, 2021.

[27] G. Kim, Y. Jung, M. Lee, E. Yoon, and S. Ahn, "SANTA: a safety analysis code for neutron absorbers in spent nuclear fuel pools," *Computer Physics Communications*, vol. 282, article 108513, 2023.

[28] B. T. Rearden and M. A. Jessee, *SCALE code system*, Oak Ridge National Lab.(ORNL), Oak Ridge, TN (United States), 2018.

[29] A. Mutzke, R. Schneider, W. Eckstein et al., *SDTrimSP version 6.00, IPP 2019-2*, Max-Planck-Institut für Plasmaphysik, 2019.

[30] J. F. Ziegler, M. D. Ziegler, and J. P. Biersack, "SRIM–the stopping and range of ions in matter (2010)," *Nuclear Instruments and Methods in Physics Research Section B: Beam Interactions with Materials and Atoms*, vol. 268, no. 11-12, pp. 1818–1823, 2010.

[31] A. Mutzke, R. Schneider, G. Bandelow, A. Mutzke, R. Schneider, and G. Bandelow, *SDTrimSP-2D: simulation of particles bombarding on a two dimensional target version 2.0, IPP 12/11*, Max-Planck-Institut für Plasmaphysik, 2013.

[32] R. Stadlmayr, P. S. Szabo, B. M. Berger et al., "Fluence dependent changes of surface morphology and sputtering yield of iron: comparison of experiments with SDTrimSP-2D," *Nuclear Instruments and Methods in Physics Research Section B: Beam Interactions with Materials and Atoms*, vol. 430, pp. 42–46, 2018.

[33] H. Hofsäss, K. Zhang, and A. Mutzke, "Simulation of ion beam sputtering with SDTrimSP, TRIDYN and SRIM," *Applied Surface Science*, vol. 310, pp. 134–141, 2014.

[34] M. J. Norgett, M. T. Robinson, and I. M. Torrens, "A proposed method of calculating displacement dose rates," *Nuclear Engineering and Design*, vol. 33, no. 1, pp. 50–54, 1975.

[35] A. Y. Konobeyev, U. Fischer, Y. A. Korovin, and S. P. Simakov, "Evaluation of effective threshold displacement energies and other data required for the calculation of advanced atomic displacement cross-sections," *Nuclear Energy and Technology*, vol. 3, no. 3, pp. 169–175, 2017.

[36] ASTM E521, *Standard Practice for Neutron Radiation Damage Simulation by Charged-Particle Irradiation, ASTM International, Annual Book of ASTM Standards*, 2009.

[37] B. Glam, S. Eliezer, D. Moreno, and D. Eliezer, "Helium bubbles formation in aluminum: bulk diffusion and near-surface diffusion using TEM observations," *Journal of Nuclear Materials*, vol. 392, no. 3, pp. 413–419, 2009.

[38] G. Ilas and I. Gauld, *Analysis of experimental data for high burnup PWR spent fuel isotopic validation-Vandellos II reactor*, Oak Ridge National Lab.(ORNL), Oak Ridge, TN (United States), 2011.

[39] F. Michel-Sendis, I. Gauld, J. S. Martinez et al., "SFCOMPO-2.0: an OECD NEA database of spent nuclear fuel isotopic assays, reactor design specifications, and operating data," *Annals of Nuclear Energy*, vol. 110, pp. 779–788, 2017.

[40] J. Marian, T. Hoang, M. Fluss, and L. L. Hsiung, "A review of helium-hydrogen synergistic effects in radiation damage observed in fusion energy steels and an interaction model to guide future understanding," *Journal of Nuclear Materials*, vol. 462, pp. 409–421, 2015.

[41] E. Hayward and C. Deo, "Synergistic effects in hydrogen–helium bubbles," *Journal of Physics: Condensed Matter*, vol. 24, no. 26, pp. 265402–265412, 2012.

[42] W. Hu, L. Guo, J. Chen et al., "Synergistic effect of helium and hydrogen for bubble swelling in reduced-activation ferritic/martensitic steel under sequential helium and hydrogen irradiation at different temperatures," *Fusion Engineering and Design*, vol. 89, no. 4, pp. 324–328, 2014.

[43] F. A. Garner, E. P. Simonen, B. M. Oliver et al., "Retention of hydrogen in fcc metals irradiated at temperatures leading to high densities of bubbles or voids," *Journal of Nuclear Materials*, vol. 356, no. 1-3, pp. 122–135, 2006.

[44] Z. Y. Fu, P. P. Liu, F. R. Wan, and Q. Zhan, "Helium and hydrogen irradiation induced hardening in CLAM steel," *Fusion Engineering and Design*, vol. 91, pp. 73–78, 2015.

[45] Y. Yang, C. Zhang, Y. Meng et al., "Nanoindentation on V-4Ti alloy irradiated by H and He ions," *Journal of Nuclear Materials*, vol. 459, pp. 1–4, 2015.